Experimental and Computational Multiphase Flow
Vol. 5, No. 4, 2023, 396–410
https://doi.org/10.1007/s42757-022-0156-4

Experimental and numerical study on the transport of dilute bubbles in a T-junction channel flow

Erik Frense[1] (✉), Xinghao Yang[1,2], Frank Rüdiger[1], Mark-Patrick Mühlhausen[2], Jochen Fröhlich[1]

1. Institute of Fluid Mechanics, Technische Universität Dresden, George-Bähr-Strasse 3c, 01069 Dresden, Germany
2. CoC Fluid Dynamics, Bosch Rexroth, Partensteiner Str. 23, 97816 Lohr am Main, Germany

Abstract

The present study investigates the transport of dilute bubbles by transitional flow in a joining, cross-flow-type T-junction channel geometry with Reynolds numbers at the outlet branch from Re_3 = 600 to 1800 and an inlet volume flow rate ratio of 1. Bubbles with diameters between d_b = 400 and 600 µm are considered. The schematic pattern of the single-phase flow is introduced based on streakline dye visualizations. Complex 3D flow due to the narrow channel design dominates the recirculation area and flow instabilities become important with increasing Reynolds number, which can be observed by the fading of dye intensity. A numerical method is presented with unsteady boundary conditions based on laser Doppler velocimetry measurements. Bubble trajectories are obtained by an Euler–Lagrange approach. Using high-speed shadowgraphy method combined with image processing, bubble sizes were measured, and bubble trajectories were evaluated. Experimental bubble trajectories and numerically predicted bubble positions show good agreement for Re_3 = 600, which is also the case with the dye visualization image. For higher Reynolds numbers, measurements of the bubble trajectories are reported and compared to dye visualization images. The increasing flow instabilities influence the bubble transport, resulting in large variations of bubble locations.

Keywords

T-junction
transitional flow
3D flow effects
streakline visualization
Euler–Lagrange method
bubble trajectories

Article History

Received: 5 August 2022
Revised: 3 December 2022
Accepted: 25 December 2022

Research Article

1 Introduction

Multiphase flow is a relevant topic in many industrial applications. In pipe systems, dissolved air can degas and form bubbles. The number and size of bubbles have an impact on system properties like the speed of sound, the compressibility or natural frequencies and influence phenomena like cavitation or boiling (Pollack, 1991; Brennen, 2005; Ruan and Burton, 2007; Gholizadeh et al., 2012). In this work, multiphase flow with a small void fraction is investigated where the bubble size spectrum can change due to bubble interaction like breakup or coalescence. For the system design, it is a key issue to predict the change in bubble size spectrum due to bubble–bubble interactions depending on the flow geometry and configuration. Many reviews on this issue can be found in literature, both for coalescence (Chesters, 1991; Kamp et al., 2001; Liao and Lucas, 2010; Hoppe and Breuer, 2018) and for breakup (Müller-Fischer et al., 2008; Liao and Lucas, 2009; Hoppe and Breuer, 2020). The models are often validated with experimental data from dispersed air in turbulent water flows, but technical applications like heat transfer technology, the flow of lubricants or hydraulic systems are characterized by a transitional flow regime due to the increased viscosity and decreased velocities. Additionally, interface behaviour may differ depending on the molecular structure of the fluid. In many cases, surfactants are added, which also has a significant effect on bubble behaviour (Takagi and Matsumoto, 2010). Overall, the basis of experimental data of fluids other than water is poor and the models validated for air–water systems can lead to errors in the description of bubble interaction.

To investigate such a complex multiphase flow, both numerical and experimental investigations are used in the present work. One goal was to define a set up representative for a configuration typically found in technical applications. In laminar to transitional flow regimes, the instabilities in

✉ erik.frense@tu-dresden.de

Nomenclature

Greek letters

μ_l	Liquid dynamic viscosity (kg/(m·s)))
ν_l	Liquid kinematic viscosity (m^2/s)
ρ_l	Liquid density (kg/m^3)
ρ_g	Gas density (kg/m^3)
σ	Surface tension (N/m)
ϕ	Phase difference (°)

Roman letters

A	Channel cross-sectional area (m^2)
C_D	Drag force coefficient
C_L	Lift force coefficient
C_{wl}	Wall force coefficient
d_b	Bubble diameter (m)
$d_{b,eq}$	Equivalent bubble diameter (m)
$d_{c,eq}$	Equivalent diameter of the channel (m)
d_p	Tracer particle diameter (m)
D	Channel depth (m)
Eo	Eötvös number
f	Frequency (Hz)
$\boldsymbol{F}_D$	Drag force vector (N)
$\boldsymbol{F}_g$	Gravity force vector (N)
$\boldsymbol{F}_L$	Lift force vector (N)
$\boldsymbol{F}_p$	Pressure gradient force vector (N)
$\boldsymbol{F}_{vm}$	Virtual mass force vector (N)
$\boldsymbol{F}_{wl}$	Wall force vector (N)
g	Acceleration magnitude due to gravity (m/s^2)
$\boldsymbol{g}$	Acceleration vector due to gravity (m/s^2)
J^*	Force coefficient factor
l_c	Cell edge length (m)
Δl	Traversing error (m)
m_b	Bubble mass (kg)
$\boldsymbol{n}_{wl}$	Unit vector perpendicular to wall
N_b	Number of pixels in a bubble
p	Liquid pressure (Pa)
P	Channel cross-sectional perimeter (m)
Re_1, Re_2, Re_3	Reynolds number at branch 1, 2, or 3
Re_b	Bubble Reynolds number
s	Spatial image resolution (m/px)
s_{wl}	Bubble to wall distance (m)
Sk_3	Stokes number
Sr	Shear number
t	Time (s)
$\dot{V}_g$	Syringe pump gas volume flow rate (m^3/s)
$\dot{V}_l$	Syringe pump liquid volume flow rate (m^3/s)
$\boldsymbol{w}$	Liquid velocity vector (m/s)
$\boldsymbol{w}_b$	Bubble velocity vector (m/s)
$\overline{w}_1$, $\overline{w}_2$, $\overline{w}_3$	Area-averaged velocity magnitude at branch 1, 2, or 3 (m/s)
w_n	Liquid velocity component normal to measurement plane (m/s)
$\langle w_n \rangle$	Time-averaged liquid velocity component normal to measurement plane (m/s)
w'_n	Variation of the liquid velocity component normal to measurement plane (m/s)
$w_{r,h}$	Relative bubble velocity component parallel to wall (m/s)
w_x, w_y, w_z	Liquid velocity components (m/s)
$\langle w_x \rangle$, $\langle w_y \rangle$, $\langle w_z \rangle$	Time-averaged liquid velocity components (m/s)
W	Channel width (m)
$\boldsymbol{x}_b$	Bubble position vector (m)
x, y, z	Coordinates (m)
Δx, Δy, Δz	Spatial errors (m)
$z_{b,i}$	Initial bubble position in z-direction (m)

Abbreviations

LDV	Laser Doppler velocimetry
CFL	Courant–Friedrichs–Lewy

straight ducts are small and bubbles interact mostly because of changes in direction predefined by the geometry and the resulting shear layers. Also, flow detachment has a strong impact on the flow instability in transitional regimes. Therefore, a joining T-junction geometry was chosen, as it is relevant in many industrial applications (Ramamurthy and Zhu, 1997; Costa et al., 2006). To guarantee the high quality of optical measurement techniques, the walls were designed planar leading to a channel geometry. To the best of the authors' knowledge, joining T-junction channel flow in transitional regime has not been well investigated. Substantial work by Patiño-Jaramillo et al. (2022) showed the flow field of two-dimensional (2D) simulations of joining T-junction laminar flow with outlet Reynolds number up to 300 for different volume flow rate ratios. Apart from the 2D limitation, higher Reynolds numbers also need to be covered.

In the present work, a test facility was designed suitable to extend the present knowledge and cover a wider range of conditions. The single-phase flow and the transport of dilute bubbles are investigated. Further studies will be concerned with the behaviour of larger bubbles and their interaction in this type of configuration.

2 Materials and methods

2.1 Model geometry and cases

The model geometry is a cross-flow-type T-junction with two inlet branches 1 and 2 and one outlet branch 3, as illustrated in Fig. 1(a). Inlet branch 1 is in the same direction as the discharging outlet branch 3 so as to form the through-going duct. It merges with inlet branch 2 under an angle of 90°. In the present work, configurations with the same volume flow rate and, therefore, the same velocity magnitude at the two inlet branches are considered. As a result, the volumetric flow rate at the outlet branch is twice that of each individual inlet. To achieve good optical access, rectangular channel geometry with plane walls was chosen. The rectangular cross-section is the same in all three channels. It has a width of $W = 25$ mm and a depth of $D = 5$ mm resulting in a hydraulically equivalent diameter of

$$d_{c,eq} = \frac{4A}{P} = 8.3 \text{ mm} \tag{1}$$

with the cross-sectional area A and the perimeter P of the channel. The origin of the coordinate system is located at the centre in the depth direction at the lower edge formed by the two inlet ducts (Fig. 1(b)). The inlet branch 1 starts at $x/W = -5$, inlet branch 2 starts at $y/W = -5$, and outlet branch 3 extends up to $x/W = 10$.

To investigate the two-phase flow, small bubbles can be introduced in controlled manner via a needle through a hole in the channel walls (Figs. 1(b) and 1(c)). These injection spots can also be used to insert high contrast dye to achieve streakline flow visualization.

For the configurations investigated in this work, the most important characteristic numbers are summarized in Table 1. The fluid velocity is characterized by the Reynolds number at the outlet branch 3:

$$Re_3 = \frac{\overline{w}_3 d_{c,eq}}{\nu_l} \tag{2}$$

with the area-averaged velocity at the outlet branch $\overline{w}_3$, the channel equivalent diameter $d_{c,eq}$, and the kinematic viscosity of the liquid ν_l. In this work, the same volume flow rate is applied at the two inlet branches so that the Reynolds numbers at branch 1 and branch 2 are $Re_1 = Re_2 = Re_3 / 2$.

The behaviour of the dispersed bubbles in the very dilute regime considered here can be described by several characteristic numbers. The bubble Reynolds number is defined as

$$Re_b = \frac{|\boldsymbol{w} - \boldsymbol{w}_b| d_b}{\nu_l} \tag{3}$$

with the velocity vector of the liquid $\boldsymbol{w}$, the velocity vector of the bubble $\boldsymbol{w}_b$, and the bubble diameter d_b. In the present study, bubbles are sufficiently small to warrant their spherical shape. Another important quantity is the Stokes number:

$$Sk_3 = \frac{\rho_g d_b^2 \overline{w}_3}{18 \nu_l \rho_l d_{c,eq}} \tag{4}$$

with the density of the gas ρ_g and the liquid ρ_l. When Sk_3 is smaller than unity, the bubbles follow the flow and no substantial slip velocity is expected. It can be seen from Table 1 that the Stokes number is orders of magnitude smaller than unity. When rising due to buoyancy, bubbles can deform if their shape is not maintained by surface tension effects. This is characterized by the Eötvös number:

$$Eo = \frac{g(\rho_l - \rho_g) d_b^2}{\sigma} \tag{5}$$

with the acceleration due to gravity g and the surface tension σ. For the cases investigated, the Eötvös number is $Eo \leq 0.1$. Hence, bubbles do not deform to a sizable extent.

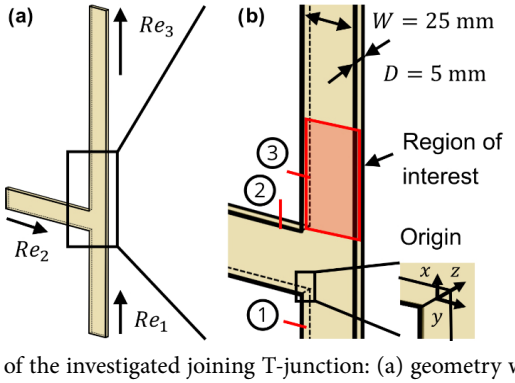

(c)

	x (mm)	y (mm)	z (mm)
①	−20	0	0
②	25	−20	0
③	45	0	0

Fig. 1 Model geometry of the investigated joining T-junction: (a) geometry with vertical inlet branch 1, horizontal inlet branch 2, and vertical outlet branch 3; (b) detailed view of the junction with marked positions of the three injection spots, geometrical dimensions of the channel cross-section, and location of the axes and their origin; (c) coordinate positions of the injection spots.

Table 1 Overview of the cases investigated, defined by Reynolds number Re_3 and bubble diameter d_b (the resulting Stokes number Sk_3 and Eötvös number Eo are provided as well)

Re_3	d_b (μm)	Sk_3 (10^{-4})	Eo
600	400	1	0.05
	500	1.6	0.07
	600	2.2	1.0
1200	400	2	0.05
	500	3.1	0.07
	600	4.5	0.1
1800	400	3	0.05
	500	4.6	0.07
	600	6.7	0.1

2.2 Experimental setup

The hydraulic scheme of the experimental facility is shown in Fig. 2(a). Each inlet of the T-junction is supplied by its own centrifugal pump (MTX 3-20, SPECK Pumpen, Germany) (1a, 1b). Additionally, and not shown in the scheme, bypasses with a directional control valve were installed upstream of the T-junction inlets to achieve an extended range of volume flow rates. Several sensors were installed to measure the volume flow rate (SU7000 or SU8000, ifm electronic, Germany) (2a, 2b), the temperature (Pt1000, otom Group, Germany) (3a, 3b, 3c), and the relative pressure (TPSI, ADZ NAGANO, Germany) (4a, 4b, 4c) at the two inlet branches, and the outlet branch, respectively.

The T-junction (5) is made of transparent polycarbonate to ensure optical accessibility. Injection spots are located at the given locations shown in Fig. 1(b), where either dye or bubbles can be injected. The latter are generated at an external microfluidic device (6c), which is shown in detail in Fig. 2(b). Bubble generation has been realized using the simple and effective concept of a cross-flow-type T-junction geometry. Basic mechanisms of bubble breakup in microfluidic devices are described in multiple works (Garstecki et al., 2006; Christopher and Anna, 2007; Drenckhan and Langevin, 2010). The bubble generation unit employed in the present study was made from a block of acrylic glass where the continuous branch and the joining branch are connected via a laser-drilled hole with a diameter of about 100 μm (Fig. 2(b)). The liquid supply of the continuous branch and the air supply of the joining branch are both driven by syringe pumps (AL-300, World Precision Instruments, USA) (6a, 6b). Preliminary studies were carried out where the size of the generated bubbles was measured when rising in a stagnant, optically accessible reservoir. The study showed that the order of magnitude of the bubble diameters is hundreds of micrometres in size depending on the volume flow rates of the air and the liquid. For the desired bubble diameters of $d_b = \{400; 500; 600\}$ μm, the ratio of liquid to gas volume flow rate had to be $\dot{V}_l/\dot{V}_g = \{60; 30; 10\}$, respectively.

Bubbles get transported via tubes from the microfluidic bubble generation unit to one of the three injection spots of the T-junction, as shown in Fig. 1(b). Downstream of the T-junction, the flow reaches the tank, which is equipped with a temperature control unit to keep the temperature at a constant level within a range of ± 3 K.

The experimental investigation of flow with and without

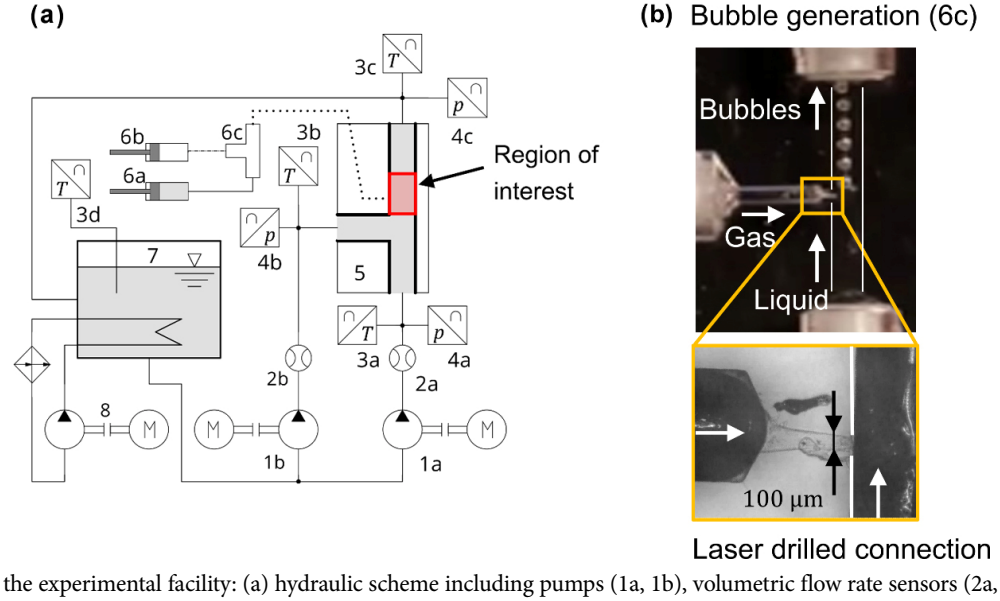

Fig. 2 Setup of the experimental facility: (a) hydraulic scheme including pumps (1a, 1b), volumetric flow rate sensors (2a, 2b), temperature sensors (3a, 3b, 3c, 3d), pressure sensors (4a, 4b, 4c), investigated T-junction (5), microfluidic bubble generation unit (6c) supplied by syringe pumps for liquid and air (6a, 6b), tank (7), and temperature control circuit (8); (b) microfluidic bubble generation unit with microscopic image of the connection between gas and liquid channel.

dilute bubbles was carried out with non-invasive optical measurement techniques. To measure the inlet velocity profile of the continuous phase, an approved laser Doppler velocimetry (LDV) system (LDV-Profile Sensor, ILA R&D GmbH, Germany) was used (Czarske et al., 2002; Nöpel et al., 2019). The system measures the absolute value of the velocity component perpendicular to the optical axis, which is the main flow direction at the inlet. A high spatial resolution of about $\Delta z = 10\,\mu\text{m}$ in the direction of the optical axis and $\Delta y = \Delta x = 50\,\mu\text{m}$ in the perpendicular directions resulting from the laser beam diameter was achieved. Silver-coated hollow glass spheres were used as tracer particles with a diameter of $d_\text{p} = 13\,\mu\text{m}$ resulting in a very small Stokes number of $Sk = \mathcal{O}(10^{-4})$.

At the inlets, the cross-section was sub-divided into 7×7 patches with a measurement point in each of them. These points were adjusted via the traversing unit for all three coordinate directions with a maximum traversing error of $\Delta l = 100\,\mu\text{m}$. Data acquisition for each point in the magnitude order of 10,000 bursts was recorded to achieve statistically converged results. Besides the mean flow velocity, the standard deviation was calculated as a measure for the variation of the velocity for each point. The arrangement of the measurement systems is shown in Fig. 3(a).

For the observation of flow without bubbles via visualization or with dilute bubbles in the region of interest, the focused high-speed shadowgraphy method was used. The setup consists of a background illumination from a white LED (LED Head - LPS v3, ILA_5150, Germany) at constant wave mode, an optical diffuser, and a high-speed camera (Phantom Miro M310, Vision Research, USA) equipped with two types of lenses for micro (Inspec.x L 105 mm, Qioptiq Photonics, Germany) and macro (Nikkor 24–85 mm, Nikon Corporation, Japan) imaging. The two lenses were chosen for two purposes: To measure the size of bubbles at the injection spots, the micro lens with a spatial resolution of 14 µm/px was used, whereas for the measurement of bubble positions and the evaluation of bubble trajectories in the region of interest, the macro lens with a spatial resolution of 67 µm/px was considered as sufficient. The temporal resolution was set in a way that the displacement of a bubble was smaller than half the diameter in between two frames. To suppress dynamic blurring of the images, the exposure time was set to the minimum sufficient value.

The focused shadowgraphy images of the dilute bubbles were evaluated via image processing to measure their size and position. For this purpose, image processing Python libraries were used, such as *scikit-image*, *trackpy*, and other basic routines (Crocker and Grier, 1996; van der Walt et al., 2014). In the first pre-processing step, a background image of a recorded sequence was extracted as the minimum pixel value across the stack and sequentially subtracted from every greyscale image. A Canny edge detection routine was used to binarize the images, followed by a routine to fill the holes which results in images with black bubbles on white background. It should be noted here that the resulting bubble size depends on the chosen threshold of the edge detection. Therefore, an overlapped image should be checked to make sure that the size of the binarized bubble fits the unprocessed bubble image (Fig. 3(b)). A manual check is an effective way to set a specific threshold, which then remains constant for the given optical setup. The number of pixels N_b of each bubble and the resolution s result in the projected bubble area $A_\text{b} = N_\text{b} s^2$. The corresponding equivalent bubble diameter was calculated from

$$d_{\text{b,eq}} = \sqrt{\frac{4A_\text{b}}{\pi}} \tag{6}$$

The bubble position corresponds to the centre of mass

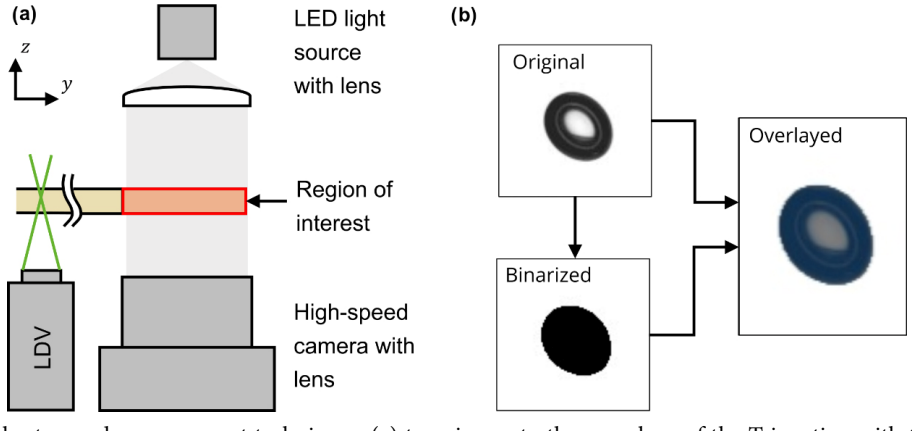

Fig. 3 Experimental setup and measurement techniques: (a) top view onto the y–z-plane of the T-junction with the region of interest marked in red. Indicated are the high-speed shadowgraphy method and the orientation of the LDV sensor head for the measurement of the inlet flow profile; (b) exemplary bubble recording overlaid with processed binary image to show the good agreement obtained with the threshold employed for the evaluation of the equivalent diameter.

of the binarized bubble area. Based on the criterion of bubble displacement between two frames not exceeding half its diameter, multiple bubble positions were linked over time to one bubble trajectory.

2.3 Numerical setup

The simulated domain includes the entire T-junction geometry, as illustrated in Fig. 1(a). It was discretized by hexahedral cells, with information on mesh quality shown in Table 2. The grid was refined by decreasing the cell width in each direction according to a given scaling factor. In addition, the change in the volume of two neighbouring cells was controlled and does not exceed 20%. Three meshes were employed for the grid independence study. The cell edge length l_c of the smallest and the largest cell in the grid is shown in Table 2 as well.

The liquid phase was computed by solving the single-phase incompressible conservation equations for mass and momentum:

$$\nabla \cdot \boldsymbol{w} = 0 \tag{7}$$

$$\frac{\partial}{\partial t}(\rho_l \boldsymbol{w}) + \nabla \cdot (\rho_l \boldsymbol{w}\boldsymbol{w}) = -\nabla p + \nabla \cdot \mu_l \left(\nabla \boldsymbol{w} + (\nabla \boldsymbol{w})^T\right) + \rho_l \boldsymbol{g} \tag{8}$$

where $\boldsymbol{w}$ and p are the liquid velocity and pressure, respectively. The density ρ_l and viscosity μ_l in Eq. (8) are the liquid properties, which are assumed to be constant. For the cases with $Re_3 = 600$, steady, laminar flow is observed in the experiment. For the other two Reynolds numbers, $Re_3 = 1200$ and $Re_3 = 1800$, the flow was found transitional in the experiment so that turbulence is not fully developed and the use of a statistical turbulence model is debatable. Hence, all three cases were simulated without a turbulence model.

The governing equations (7) and (8) of the liquid phase were solved in transient mode using Ansys Fluent v20.2. The spatial derivatives were discretized using a third-order MUSCL scheme, and pressure interpolation was done by PRESTO!. Temporal derivatives were discretized with a second-order implicit scheme. The convergence criterion for all equations was to require that the scaled residuals have decreased to 10^{-5}.

First, a mesh independence study was performed for $Re_3 = 1800$ with steady boundary conditions at the inlet and outlet. The time-averaged results along four lines are compared with each other in Fig. 4. The near-wall velocity values on the coarse grid in Figs. 4(d), 4(e), and 4(f) are astonishingly large, but this was proven to be an artefact of the extraction procedure by the commercial post-processing tool. The results obtained in this study show no significant difference between medium-size mesh and fine mesh. Hence, the medium-size mesh was used for the bulk of the simulations.

Single-phase simulations were conducted for two Reynolds numbers $Re_3 = 600$ and 1800. In the experiment, the velocity profiles at the two inlets were measured by LDV. These profiles were used to define the inlet boundary conditions. Since the measured points do not coincide with the numerical face centres at the inlet boundary, a 2D interpolation was performed to compute the numerical velocity profiles at the grid points located in the inlet planes. Barycentric interpolation was used, as illustrated in Fig. 5.

The measured velocity at the inlet varies in time due to fluctuations in the pipe system, as discussed in Section 3.3. In order not to miss any trigger for a potential instability in the flow, the inflow condition was prescribed in an unsteady way, imposing a pulsating profile at both inlets. To this end, the instantaneous velocity w_n normal to the inlet face was imposed at each grid point of the two inlet planes according to

$$w_n = \langle w_n \rangle + \sqrt{\langle w'_n w'_n \rangle}\sqrt{2}\sin(ft + \phi) \tag{9}$$

with t the time, f the frequency, and ϕ indicating the phase difference between inlet 1 and inlet 2. The frequency $f = 50$ Hz was motivated by the rotational speed of the pump upstream of the inlet. The quantities $\langle w_n \rangle$ and $\sqrt{\langle w'_n w'_n \rangle}$ in Eq. (9) denote the experimentally measured mean flow and standard deviation, respectively, evaluated at the given position. Zero viscous flux was imposed at the outlet, and no-slip condition was used at the walls. In all simulations, the maximal Courant–Friedrichs–Lewy (CFL) number was smaller than 1. Statistical quantities of the fluid velocity field were computed from the unsteady simulation after a sufficiently long start-up period.

The bubble velocity was computed by solving an ordinary differential equation for the linear momentum

Table 2 Mesh quality for grid independence study

Name	Cell number	Scale factor	Max. volume change	Max. aspect ratio ($0 < x/W < 3$)	Smallest cell l_c (mm)	Largest cell l_c (mm)
Coarse	2 million	1	1.13	4.05	0.25	0.4
Medium	4.5 million	1.3	1.1	6.86	0.063	0.46
Fine	8.4 million	1.62	1.2	6.65	0.042	0.37

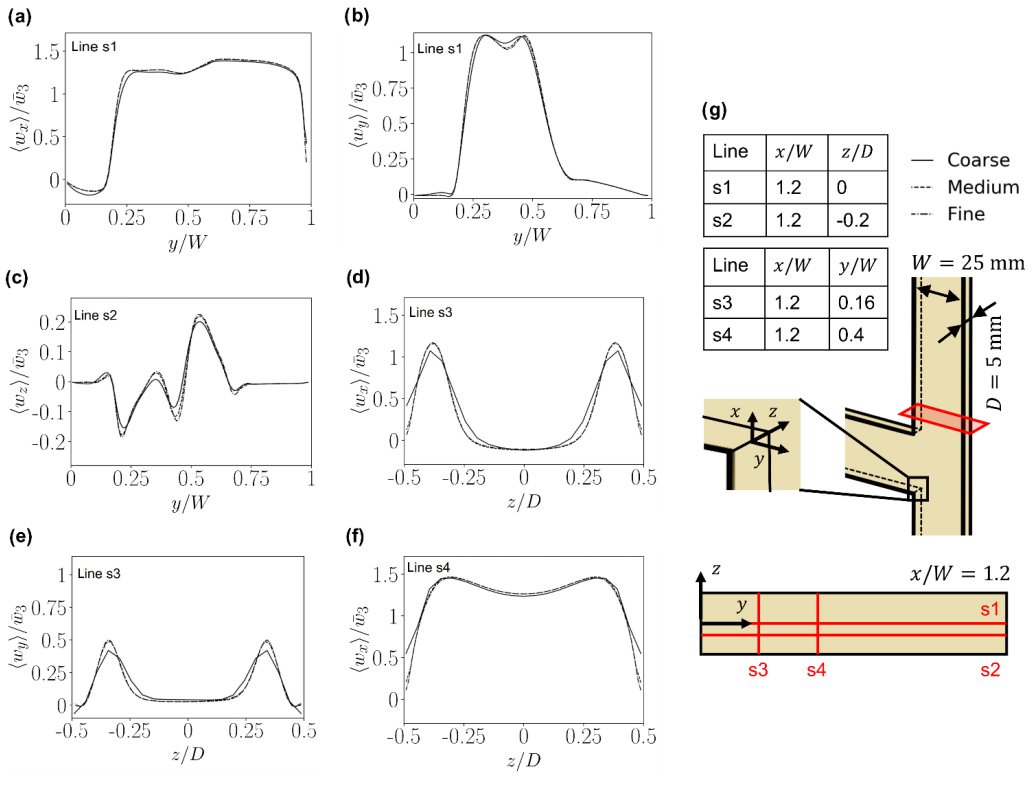

Fig. 4 Mesh independency study for time-averaged liquid velocity along selected lines (s1 to s4) indicated in the right part of the figure.

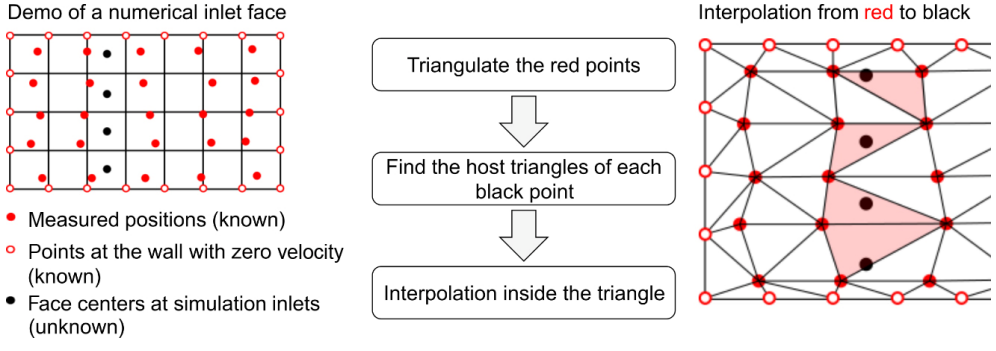

Fig. 5 Barycentric interpolation to obtain the velocity at the grid points in the inflow plane from the measured velocity.

considering different forces on the bubble. Generally, these forces may be divided into fluid dynamic forces (e.g., drag, pressure, virtual mass, Saffman forces, etc.) and field forces (gravity, electrostatic forces, etc.). Hence, the equations of motion for each bubble read

$$\frac{\mathrm{d}\boldsymbol{x}_\mathrm{b}}{\mathrm{d}t} = \boldsymbol{w}_\mathrm{b} \tag{10}$$

$$m_\mathrm{b}\frac{\mathrm{d}\boldsymbol{x}_\mathrm{b}}{\mathrm{d}t} = \boldsymbol{F}_\mathrm{D} + \boldsymbol{F}_\mathrm{vm} + \boldsymbol{F}_\mathrm{P} + \boldsymbol{F}_\mathrm{g} + \boldsymbol{F}_\mathrm{L} + \boldsymbol{F}_\mathrm{wl} \tag{11}$$

where $\boldsymbol{x}_\mathrm{b}$ is the bubble position vector and $\boldsymbol{w}_\mathrm{b}$ is the bubble velocity vector. The forces on the right-hand side of Eq. (11) are drag force, virtual mass force, pressure gradient force, gravity, lift force, and the wall force, respectively. Compared to the models used by Yang et al. (2021a, 2021b), different drag and lift force coefficients were employed here, and the wall force was considered as well. For the convenience of the reader, all modelling terms employed are recalled here. For the drag force, it is important to recall that the liquid is generally contaminated by surfactants. As a result, the drag force coefficient C_D is the one for contaminated bubbles (Tomiyama et al., 1998):

$$C_\mathrm{D} = \max\left\{\frac{24}{Re_\mathrm{b}}\left(1+0.15Re_\mathrm{b}^{0.687}\right), \frac{8Eo}{3\left(Eo+4\right)}\right\} \tag{12}$$

It is found that the Eötvös number remains small, i.e., $Eo < 0.3$, due to the small size of bubbles. In this case, the lift correlation of Legendre and Magnaudet (1998):

$$C_{\mathrm{L}}=\sqrt{\left(\frac{11+16/Re_{\mathrm{b}}}{21+29/Re_{\mathrm{b}}}\right)^{2}+\left[\frac{6}{\pi^{2}}\left(Re_{\mathrm{b}}Sr\right)^{-0.5}J'\right]^{2}} \tag{13}$$

is suitable to determine the Saffman lift force $\boldsymbol{F}_{\mathrm{L}}$, where

$$J'=\frac{2.255}{\left(1+0.2Re_{\mathrm{b}}/Sr\right)^{1.5}} \tag{14}$$

$$Sr=d_{\mathrm{b}}\frac{|\nabla\times\boldsymbol{w}|}{|\boldsymbol{w}-\boldsymbol{w}_{\mathrm{b}}|} \tag{15}$$

It is valid for bubbly flows with $0.1\le Re_{\mathrm{b}}\le 500$ and $0\le Sr\le 1$.

The wall force $\boldsymbol{F}_{\mathrm{wl}}$ plays a significant role for bubbles moving in wall-bounded flows. The model employed for $\boldsymbol{F}_{\mathrm{wl}}$ reads

$$\boldsymbol{F}_{\mathrm{wl}}=m_{\mathrm{b}}C_{\mathrm{wl}}\frac{6}{4d_{\mathrm{b}}}\frac{\rho_{\mathrm{l}}}{\rho_{\mathrm{g}}}w_{\mathrm{r,h}}^{2}\boldsymbol{n}_{\mathrm{wl}} \tag{16}$$

where C_{wl} is the wall force coefficient (Takemura and Magnaudet, 2003). The symbols are defined in Fig. 6. The velocity $w_{\mathrm{r,h}}$ is the relative velocity parallel to the wall. The distance between the wall and the bubble center is denoted as s_{wl}. The direction of the wall force is defined by $\boldsymbol{n}_{\mathrm{wl}}$, which is the unit vector perpendicular to the wall pointing into the fluid. In an upward flow such as the one in Fig. 6, the Saffman lift force pushes the bubble towards the wall while the wall force acts in the opposite direction.

Additional to the forces mentioned above, a soft-sphere elastic collision force was employed between the bubbles and the walls. This force is enabled only when s_{wl} is smaller than the bubble radius. The equation of this force can be found in Heitkam et al. (2017).

Only one-way coupling is considered here due to the small number and the small size of bubbles in this work. Bubble–bubble interaction and bubble breakup are not modelled as these do not occur in the corresponding experiments.

Bubble trajectories at a Reynolds number of $Re_3=600$ were simulated based on the converged single-phase solution at the last time step, i.e., with a steady velocity field very close to the average flow field. No instabilities occurred in the flow, so this is the desired flow field. In fact, $Re_3=600$ is far below the critical value of transition to turbulent flow, so the effect of turbulent dispersion of bubbles can be ignored.

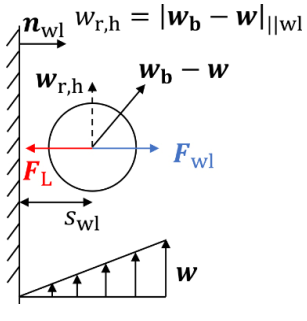

Fig. 6 Illustration of the wall-lift force in an upward flow.

In the simulation, bubbles with a given diameter were released from the injection spot 3. The initial distance between the wall and the bubble centre is equal to the bubble radius. Four bubble trajectories were computed simultaneously. The initial z-coordinates of the four bubble centres are $z_{\mathrm{b,i}}\in\{-0.04;-0.02;0.02;0.04\}$mm to consider the effect of asymmetric bubble injection in the experimental setup. Nevertheless, modifying the initial bubble velocity in the same order of magnitude does not affect the subsequent trajectory due to the small bubble Stokes number. The bubble almost immediately adopts the velocity of the surrounding fluid.

3 Investigation of single-phase flow

3.1 Schematic flow pattern and 3D effects from numerical simulation

In this section, schematic flow characteristics are discussed aiming at a better understanding of the flow in terms of 3D structures. Simulations of the single-phase flow were carried out to study the schematic flow pattern of the joining T-junction with rectangular channel cross-section illustrated in Fig. 1. Essential results are reported in Fig. 7. The first part, Fig. 7(a), shows 2D streamlines of the x–y plane in the centre plane at $z=0$ superimposed with normalized velocity vectors. The detachment zone at the lower connecting edge of branch 1 and branch 2 is marked with region (I). The flow structure in this region is illustrated in detail in Fig. 7(b) with a front view showing the x–y plane and a side view from a 90° angle showing the x–z plane. 3D streamlines are coloured in orange when starting in branch 1 and coloured in blue when starting from branch 2 at a near wall position where the injection spots are located. Orange streamlines intrude the lower pressure zone in negative y-direction into the detachment zone of branch 2 and mix with the blue streamlines coming from branch 2. The side view shows the displacement of the streamlines towards the front and back wall in z-direction. This illustrates the highly 3D nature of the flow at the lower corner of the branch, with a substantial quantity of fluid being diverted from the centre plane to the lateral walls.

In Fig. 7(c), 2D streamlines are shown with superimposed normalized velocity vectors in the z–y plane from the top view of region (II) at a given location marked in Fig. 7(a).

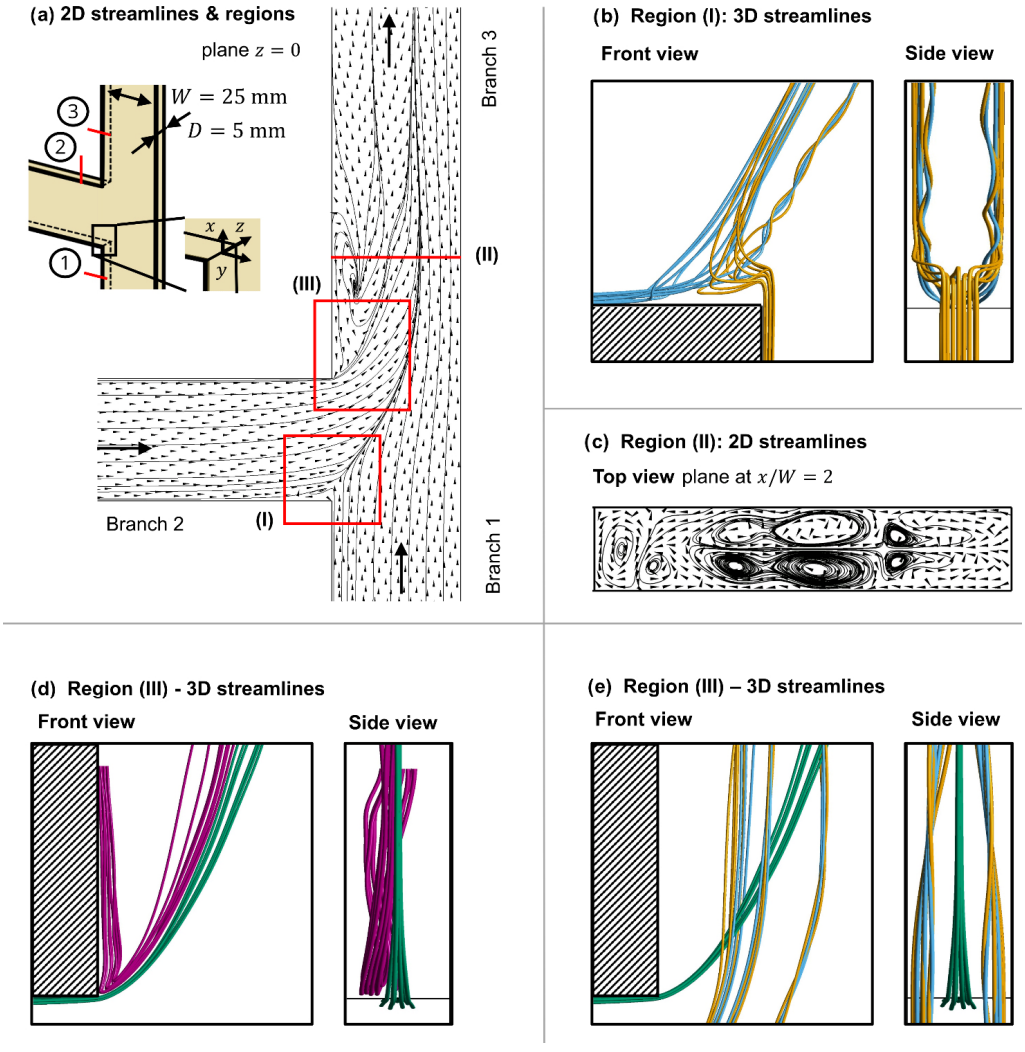

Fig. 7 Schematic illustration of the single-phase flow in the T-junction obtained from numerical simulation: (a) 2D streamlines in the x–y plane at $z = 0$ superimposed with normalized velocity vectors. The figure also highlights different regions discussed in the text: Region (I)—detachment zone at the connecting edge of branch 1 and 2, region (II)—location of the top view in the recirculation area, and region (III)—detachment zone at the connecting edge of branch 2 and 3; (b) front view (view in z-direction) and side view (view in negative y-direction) of region (I) showing 3D streamlines. They start at a near-wall position in branch 1 (orange) and in branch 2 (blue); (c) top view of region (II) displaying 2D streamlines in the plane $x/W = 2$ superimposed with normalized velocity vectors; (d) front and side view of region (III) showing 3D streamlines starting from a near-wall position in branch 2 (green) and in branch 3 (purple); (e) front and side view of region (III) with 3D streamlines from branch 1 (orange and blue) and branch 2 (green).

Several secondary vortices from the lower corner are created by the 3D flow effects but are not discussed in detail here.

The schematic flow pattern in region (III), located around the upper corner of the junction, is shown in Figs. 7(d) and 7(e). The 3D streamlines coloured in green starting at the injection spot 2 illustrate the detachment of the flow from branch 2 when entering branch 3 which is caused by the abrupt change of the contour. The detached flow drives a recirculation area in branch 3 along the wall forming the corner with branch 2. 3D effects drive these streamlines towards the centre plane, as shown in the side view. 3D streamlines were also started at a near wall position at the injection spot 3, shown in purple. The visualization shows that the flow is orientated downward at the injection spot, opposed to the main flow in the branch, so that these streamlines move to the upper corner of the junction. Deviations from the vertical motion are small and generated by tiny asymmetries of the flow. The streamlines introduced near injection spot 3 remain inside the recirculation zone and constitute the inward part of the shear layer forming at the border with the outer, non-recirculating flow (cf. Fig. 7(a)). Hence, bubbles simultaneously injected into both injection spots 2 and 3 would meet and interact in this region. Figure 7(a) illustrates that the recirculation area reattaches back to the wall downstream of the junction, in branch 3. In Fig. 7(e), the location of the streamlines

introduced at branch 1 and the bottom wall of branch 2 marked in orange and blue are shown, together with the green ones from branch 2 as a reference. Both sets of streamlines pass the recirculation area in different locations in z-direction. The ones from branch 1 are diverted towards the lateral walls by the 3D flow effects and are slightly twisted and at the same time driven somewhat inward, as can be appreciated from the side view.

The visualizations reveal part of the complex 3D flow pattern, into which the bubbles are released in this experiment. Combined with the presumption of more bubble interactions in regions with present shear layer flow, the focus in this work lies in the investigation of region (III). Here, bubbles coming from both inlet branches are likely to interact with each other, allowing interaction of similar but also different types of bubbles to take place.

3.2 Flow visualization in the experiment

To validate the numerical results of Section 3.1 and to gain further information on the complex 3D flow, streakline visualization experiments were carried out. This provides single-phase flow behaviour and highlights mean flow and variations, if any. Coloured fluid was injected through the injection spots described in Section 2.1 and recorded by focused shadowgraphy. For this purpose, red pepper powder (Paprika rosenscharf L9170BD, Ostmann Gewürze, Germany) was resolved in the fluid and injected via the injection spot in branch 3 at $x/W = 1.8$ directly into the recirculation area. A good contrast was achieved and clear streakline visualization for various Reynolds numbers was obtained, as shown in Fig. 8. Analogous to the purple streamlines introduced in the numerical solution (Fig. 7(d)), the dye in the experiment gets transported near the wall in negative x-direction towards the detachment zone. The coloured streakline follows the border of the recirculation area and does not reattach to the wall because of the 3D secondary flow effects discussed in Section 3.1. This agrees very well with the numerical observations. For increased Reynolds numbers, the variation of the flow velocity yields a fading of the contrast as a result of small-scale mixing with the uncoloured fluid (Fig. 8). Furthermore, coloured fluid gets transported into an increasing portion of the recirculation area. Overall, no reattachment of the flow downstream of the recirculation area is detectable for increased Reynolds numbers. It is expected that the 3D effects and secondary flow phenomena play an important role for the transport of bubbles.

3.3 Measurement of boundary conditions

For the comparison between numerical and experimental results, it is essential to have the same boundary conditions. To provide the inlet condition for the simulation, the velocity component normal to a plane very close to the inlet was measured using LDV, as shown in Fig. 9(a). The velocity is termed w_n here, with $w_n = w_x$ for inlet 1 and $w_n = w_y$ for inlet 2, and was collected for $Re_3 \in \{600; 1200; 1800\}$. As an example, Fig. 9(b) shows isolines of the dimensionless mean velocity $w_n/\overline{w}$ for the inlet branch 2, where $\overline{w}$ is the area-averaged velocity for the corresponding Reynolds number.

The isolines in Fig. 9(b) show that with increasing Reynolds number, the streamwise velocity in the inlet exhibits an increasing gradient near the wall and a widened flat region in the centre. This is illustrated here only for $Re_3 = 1800$ in Fig. 9(c). The inlet velocity profile is the result of the flow conditioning consisting of a nozzle, combined

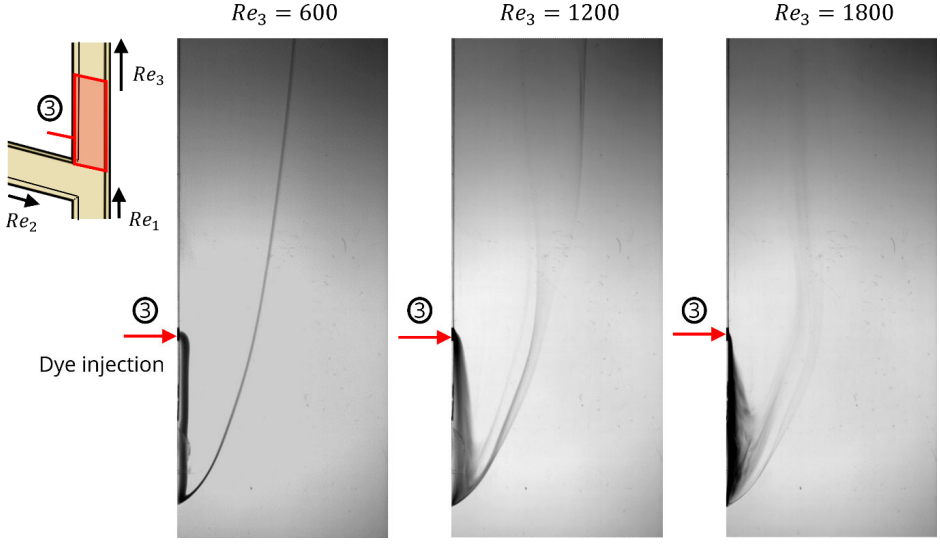

Fig. 8 Shadowgraphy images of dye visualization with marked injection spot 3 for various Reynolds numbers.

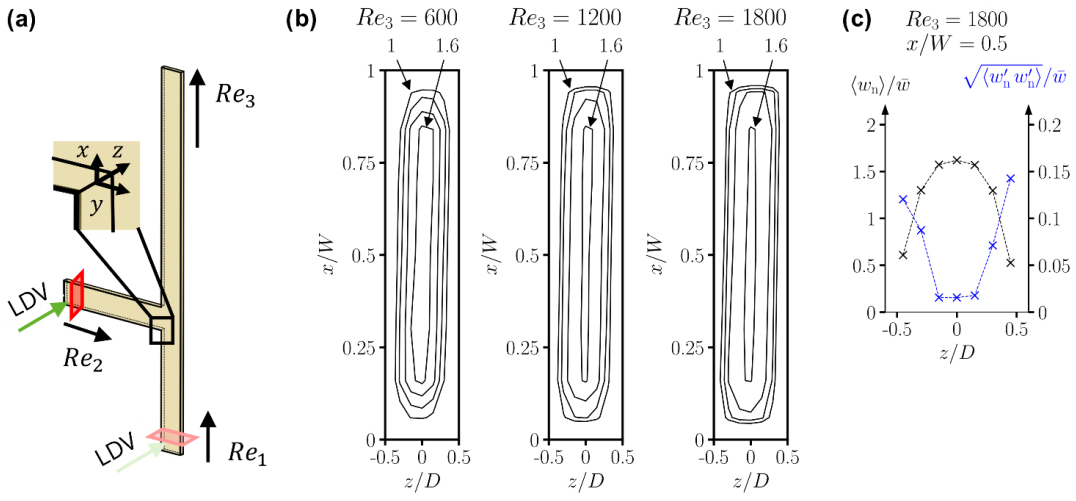

Fig. 9 Flow at the inlet boundary, face 2, measured with LDV: (a) location of measurement plane (red) at $y/W = -4.4$; (b) isolines of the normalized mean velocity $\langle w_n \rangle / \bar{w} \in \{1; 1.2; 1.4; 1.6\}$ for the three Reynolds numbers $Re_3 \in \{600; 1200; 1800\}$ with the inner and outer isolines annotated in the diagram; (c) cut through the velocity field for $Re_3 = 1800$ at $y/W = -4.4$ shown in part (a). Profiles of the mean velocity $\langle w_n \rangle / \bar{w}$ and the velocity variation $\sqrt{\langle w'_n w'_n \rangle}/\bar{w}$ are shown along a line $x/W = 0.5$ using a set of regularly distributed points, connected with dashed lines to guide the eye.

with a change in cross-sectional shape from round to rectangular, mostly with a change in z-direction directly upstream of the measurement plane. This yields a well-advanced developed flow profile in z-direction and a nearly constant block-profile in x-direction. The conditioning of the first inlet branch was identical. The very slight asymmetry of the velocity profile can be explained by either the hydraulic components upstream the model geometry or uncertainties in the arrangement of the LDV sensor head.

The evaluation of the standard deviation $\sqrt{\langle w'_n w'_n \rangle}$, with $w'_n = w_n - \langle w_n \rangle$, gives a measure for the streamwise variations on the inflow plane. Variations increase towards the channel wall (Fig. 9(c)). At this region, systematic uncertainties of near-wall optical measurements and transient effects of the flow cannot be neglected.

The data shown here were used to formulate transient boundary conditions for the numerical simulations described in Section 2.3. This enables the transient effects like pulsation from the experimental setup. Velocity variations could also emerge from transient shifting and deformation of the profile without any pulsation of the volume flow rate. Accounting for these effects in an unsteady inlet boundary condition would require a much more sophisticated model and more experimental data.

4 Investigation of two-phase flow

4.1 Quantification of bubble injection

Bubble generation by the microfluidic unit was devised and tested with still fluid as described in Section 2.2. Since the cross flow can, in principle, have an impact on the properties of the bubbles injected, injection into the developed flow was investigated again using high-speed shadowgraphy images. Figure 10 shows a sample picture taken at the injection spot of branch 2. Several bubbles are visible which have all been unleashed at the injection spot one after the other.

The image processing routines to evaluate the bubble diameter described in Section 2.2 were applied to each bubble in each frame of the sequence. And then, averaging was performed over the diameter values determined in different frames for the same bubble and over different bubbles. This resulted in the mean equivalent bubble diameter and its standard deviation for a given configuration. The data are reported in Table 3 for the three Reynolds numbers and volume flow rate ratios set at the syringe pumps.

The bubble sizes are in the range of the nominal values of $d_b = \{400; 500; 600\}$ µm, and the change in diameter for each volume flow rate ratio is sufficiently small compared to the size of the bubbles. For higher Reynolds numbers, bubbles with increased diameter deform towards an ellipsoidal shape due to the shear layer at the injection spot

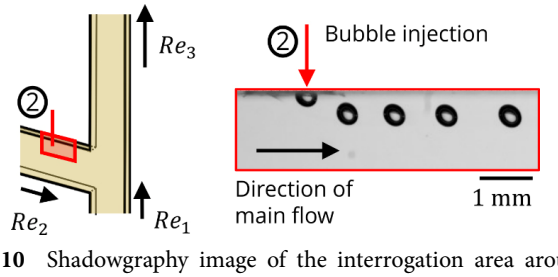

Fig. 10 Shadowgraphy image of the interrogation area around injection spot 2 indicated in the left sketch, with only part of the channel height covered, for $Re_3 = 600$ and $\dot{V}_l/\dot{V}_g = 60$.

Table 3 Measured mean equivalent bubble diameter $d_{b,eq}$ (μm) and standard deviation at injection spot 2 for different flow configurations and pre-defined volume flow rates ratios set at the syringe pumps

Re_3 \ $\dot{V}_l/\dot{V}_g$	60	30	10
600	381 ± 8	482 ± 9	686 ± 9
1200	370 ± 14	470 ± 18	670 ± 11
1800	370 ± 18	460 ± 20	580 ± 80

acting against the surface tension force, which is too small to obtain a spherical shape. The deformation yields an increase in the standard deviation because the shape also changes in z-direction, i.e., in depth, resulting in a variation of the projected area. Although efforts were made to meet the nominal diameter, further efforts might lead to an even better match. On the other hand, the results below show that the bubble diameter is of little influence in the range considered.

4.2 Trajectories of bubbles

To investigate the transport of dilute bubbles in the T-junction flow, the trajectories of the bubbles were evaluated using the image processing routine described in Section 2.2. Bubbles were introduced into the recirculation area via the injection spot in branch 3. The trajectories for $Re_3 = 600$ and various bubble diameters are shown in Fig. 11 by the dark blue line, which is the union of many centre point locations, all superimposed. The bubbles get transported in negative x-direction, driven by the near-wall flow in the recirculation area. After reaching the bottom of the recirculation area, the bubbles accelerate at the boundary of the recirculation zone. As discussed above, there is no reattachment of bubble paths because of 3D effects. Figure 11 also shows the calculated trajectories from the simulations in the form of red dots.

Good agreement between the experimental bubble trajectories and the numerical results can be seen with only little effect of the bubble size. The tiny differences may result from very small differences in the experimental and the numerical flow field. The geometry of the computational domain was modelled with sharp edges, for example, whereas the real channel geometry has small radii at the edges. Together with the model of the inflow conditions this may result in a small shift of the 3D flow structures.

In addition to the bubble trajectories, an image from the dye visualization was inserted at the background in Fig. 11. The trajectories and the streakline separate downstream in the upper region of the investigated area. Buoyancy effects have little influence here as the velocity of the bubbles is approximately two orders of magnitude higher than the rising velocity in stagnant fluid. Still, the trajectories of the larger bubbles are slightly steeper in the graphs. Overall, only very small differences between bubble transport and continuous flow are detectable in the results, indicating that one-way coupling is a suitable approach for the simulations. The bubble locations are predicted well by the simulation method.

For higher Reynolds numbers, no simulations were conducted. The experiments show that flow instabilities are increasing, which leads to a significant variation of bubble locations. In Fig. 12, trajectories from experiments are superimposed with the corresponding dye visualization images of Fig. 8. For $Re_3 = 1200$, the bubbles are transported in negative x-direction towards the separation zone of the recirculation area. Bubbles are located at an increased distance

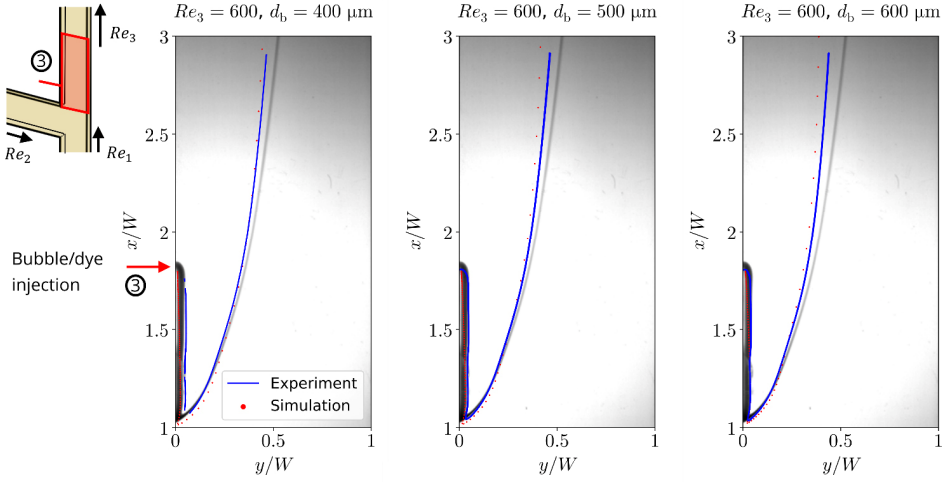

Fig. 11 Numerically predicted bubble trajectories for three different bubble diameters (red dots) superimposed with the corresponding experimentally determined bubble trajectories (dark blue line) for $Re_3 = 600$. These two datasets are overlaid with the corresponding streamline plot of Fig. 8 containing the grey streakline.

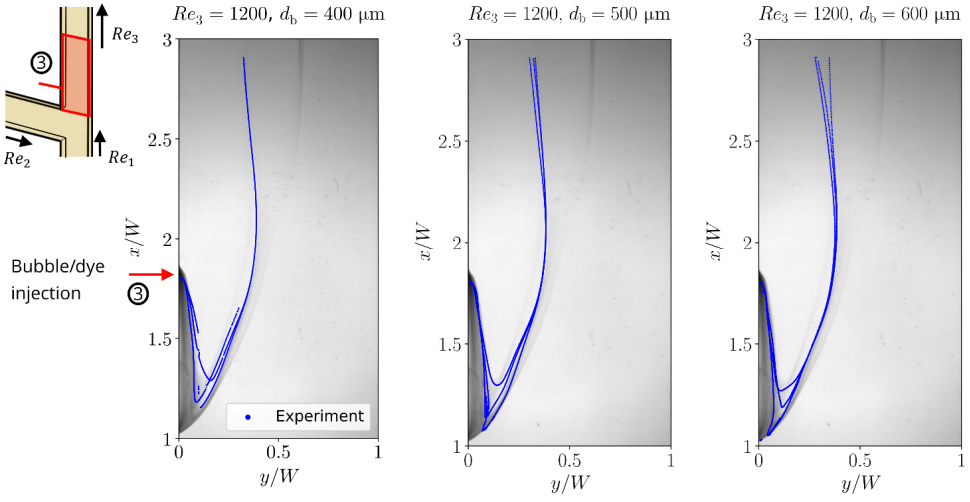

Fig. 12 Experimentally measured trajectories for $Re_3 = 1200$ for three different bubble diameters in the investigation area superimposed with dye visualization images.

normal to the wall compared to dye-filled region, which indicates a resulting force component pointing away from the wall. Multiple single trajectories can be seen due to flow instabilities in that region. Downstream of the recirculation area, at $x/W \approx 2$, the streakline from dye visualization and the bubble trajectories are separating and the bubbles get transported in negative y-direction. This indicates an influence of the 3D flow effects.

For $Re_3 = 1800$ (Fig. 13), increasing flow instabilities lead to a higher variation in bubble trajectories, which can be seen from the existence of a large number of different trajectories of different bubbles. Inspection of photographs (not reproduced here) shows that for $Re_3 = 1800$ and $d_b = 600$ µm increased bubble deformation occurs. Even bubble breakup is occasionally observed directly at the injection spot, generating two bubbles in a highly unstable flow field. As a result, bubbles can be found in the whole recirculation area.

5 Conclusions

The understanding of bubble interaction is important to predict system properties for transitional flow. A cross-flow-type T-junction geometry was chosen as a reference configuration and a test facility devised. Experimental results were presented for Reynolds numbers at the outlet ranging from $Re_3 = 600$ to 1800.

The single-phase flow was simulated by a numerical model with boundary conditions obtained from the experimental facility. For this purpose, the velocity profile at the inlet faces was measured with LDV and implemented as an unsteady inflow condition. The schematic flow pattern

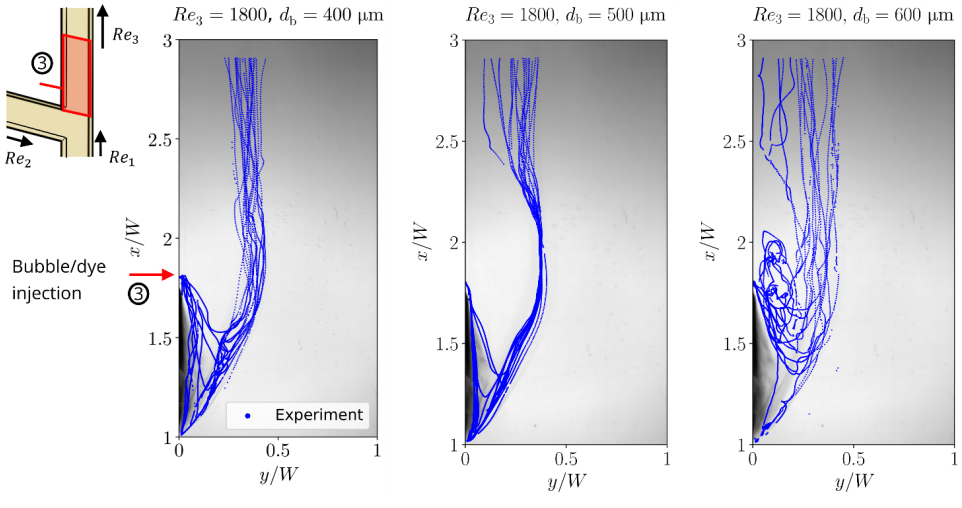

Fig. 13 Experimentally measured trajectories for $Re_3 = 1800$ for three different bubble diameters in the investigation area superimposed with dye visualization images.

and the 3D effects of the joining T-junction channel flow were elucidated using streamlines from the simulation and streakline images from dye visualization experiments. In the region of interest, the recirculation area is influenced by 3D effects which dominate bubble transport.

Subsequently, bubbles were injected into the T-junction flow. The properties of the injected bubbles in the experiment were evaluated using high-speed shadowgraphy imaging. Bubbles with adjustable diameters from $d_{b,eq} = 400$ to 600 µm were generated by a bubble generation unit and introduced to the main flow via injection spots. Directly after the injection, the bubble sizes were evaluated using image processing, where a good agreement with preliminary studies was achieved. It was shown that the equivalent bubble diameter remains sufficiently constant for various Reynolds numbers.

The numerical model was enhanced by a Lagrangian description of the bubbles in the very dilute regime considered, using one-way coupling. Calculated bubble trajectories from the simulation were compared with experimental results for $Re_3 = 600$ without significant differences on the predicted bubble locations, also regarding the single-phase flow represented by the dye visualization image. This demonstrates the applicability of one-way coupling in this case.

For higher Reynolds number, the contrast of the dye visualization imaging was fading due to mixing with non-colorized fluid which is enhanced by flow instabilities. Unsteady velocity variations of the flow field are also reason for the variation of measured bubble trajectories. Hence, the transport is dominated by the unsteady 3D effects of the continuous phase.

In the present experiment, bubbles were injected into complex 3D flow, but the behaviour was described only by evaluating 2D information from the imaging. The use of stereo imaging gives additional information and is presently used in ongoing work. Present work is also concerned with the description of the bubble deformation induced by the surrounding flow. To this end, the strength of the shear layer at the border of the recirculation area is influenced by selecting appropriate Reynolds numbers and volume flow rate ratios of the two inlet branches which was unity for now.

The next step will be to investigate bubble–bubble and bubble–fluid interactions like collision, coalescence, and breakup. Simultaneous injection of bubbles into the injection spots of branch 2 and branch 3 can lead to bubble–bubble encounters as indicated by the 3D streamline visualization. To detect and analyse interaction events, it is necessary to develop further image processing routines which have been presented by Frense et al. (2022). This enables the automatic evaluation of interactions to increase the data basis for statistical modelling with a big number of interaction events. Ultimately, the data will be used to validate bubble interaction models for configurations found in typical industrial applications.

Funding note

Open Access funding enabled and organized by Projekt DEAL.

Declaration of competing interest

The authors have no competing interests to declare that are relevant to the content of this article.

References

Brennen, C. E. 2005. *Fundamentals of Multiphase Flow*. Cambridge: Cambridge University Press.

Chesters, A. 1991. The modelling of coalescence processes in fluid–liquid dispersions: A review of current understanding. *Chemical Engineering Research & Design*, 69: 259–270.

Christopher, G. F., Anna, S. L. 2007. Microfluidic methods for generating continuous droplet streams. *Journal of Physics D: Applied Physics*, 40: R319–R336.

Costa, N. P., Maia, R., Proença, M. F., Pinho, F. T. 2006. Edge effects on the flow characteristics in a 90 deg tee junction. *Journal of Fluids Engineering*, 128: 1204–1217.

Crocker, J. C., Grier, D. G. 1996. Methods of digital video microscopy for colloidal studies. *Journal of Colloid and Interface Science*, 179: 298–310.

Czarske, J. R., Büttner, L., Razik, T., Müller, H. 2002. Boundary layer velocity measurements by a laser Doppler profile sensor with micrometre spatial resolution. *Measurement Science and Technology*, 13: 1979–1989.

Drenckhan, W., Langevin, D. 2010. Monodisperse foams in one to three dimensions. *Current Opinion in Colloid & Interface Science*, 15: 341–358.

Frense, E., Werner, T., Nöpel, J.-A., Rüdiger, F. 2022. Detection and evaluation of single bubble collisions using focused shadowgraphy. In: Proceedings of the 29th Symposium of Experimental Fluid Mechanics of GALA e.V., 17.4–17.8. Available at https://www.gala-ev.org/images/Beitraege/Beitraege2022/pdf/17.pdf.

Garstecki, P., Fuerstman, M. J., Stone, H. A., Whitesides, G. M. 2006. Formation of droplets and bubbles in a microfluidic T-junction-scaling and mechanism of break-up. *Lab Chip*, 6: 437–446.

Gholizadeh, H., Burton, R., Schoenau, G. 2012. Fluid bulk modulus: Comparison of low pressure models. *International Journal of Fluid Power*, 13: 7–16.

Heitkam, S., Sommer, A. E., Drenckhan, W., Fröhlich, J. 2017. A simple collision model for small bubbles. *Journal of Physics: Condensed Matter*, 29: 124005.

Hoppe, F., Breuer, M. 2018. A deterministic and viable coalescence model for Euler–Lagrange simulations of turbulent microbubble-laden flows. *International Journal of Multiphase Flow*, 99: 213–230.

Hoppe, F., Breuer, M. 2020. A deterministic breakup model for Euler–Lagrange simulations of turbulent microbubble-laden flows. *International Journal of Multiphase Flow*, 123: 103119.

Kamp, A. M., Chesters, A. K., Colin, C., Fabre, J. 2001. Bubble coalescence in turbulent flows: A mechanistic model for turbulence-induced coalescence applied to microgravity bubbly pipe flow. *International Journal of Multiphase Flow*, 27: 1363–1396.

Legendre, D., Magnaudet, J. 1998. The lift force on a spherical bubble in a viscous linear shear flow. *Journal of Fluid Mechanics*, 368: 81–126.

Liao, Y., Lucas, D. 2009. A literature review of theoretical models for drop and bubble breakup in turbulent dispersions. *Chemical Engineering Science*, 64: 3389–3406.

Liao, Y., Lucas, D. 2010. A literature review on mechanisms and models for the coalescence process of fluid particles. *Chemical Engineering Science*, 65: 2851–2864.

Müller-Fischer, N., Tobler, P., Dressler, M., Fischer, P., Windhab, E. J. 2008. Single bubble deformation and breakup in simple shear flow. *Experiments in Fluids*, 45: 917–926.

Nöpel, J. A., Frense, E., Korb, S., Dues, M., Rüdiger, F. 2019. Velocity measurement of a free jet in water with shear layer cavitation. In: Proceedings of the 27th Symposium of Experimental Fluid Mechanics of GALA e.V., 38.1–38.8. Available at https://www.gala-ev.org/images/Beitraege/Beitraege2019/pdf/38.pdf.

Patiño-Jaramillo, G. A., Iglesias, I., Vera, M. 2022. Laminar flow and pressure loss in planar Tee joints: Numerical simulations and flow analysis. *European Journal of Mechanics - B/Fluids*, 92: 75–89.

Pollack, G. L. 1991. Why gases dissolve in liquids. *Science*, 251: 1323–1330.

Ramamurthy, A. S., Zhu, W. 1997. Combining flows in 90° junctions of rectangular closed conduits. *Journal of Hydraulic Engineering*, 123: 1012–1019.

Ruan, J., Burton, R. 2007. Bulk modulus of air content oil in a hydraulic cylinder. In: Proceedings of the ASME 2006 International Mechanical Engineering Congress and Exposition, 259–269.

Takagi, S., Matsumoto, Y. 2010. Surfactant effects on bubble motion and bubbly flows. *Annual Review of Fluid Mechanics*, 43: 615–636.

Takemura, F., Magnaudet, J. 2003. The transverse force on clean and contaminated bubbles rising near a vertical wall at moderate Reynolds number. *Journal of Fluid Mechanics*, 495: 235–253.

Tomiyama, A., Kataoka, I., Zun, I., Sakaguchi, T. 1998. Drag coefficients of single bubbles under normal and micro gravity conditions. *JSME International Journal Series B*, *Fluids and Thermal Engineering*, 41: 472–479.

Van der Walt, S., Schönberger, J. L., Nunez-Iglesias, J., Boulogne, F., Warner, J. D., Yager, N., Gouillart, E., Yu, T. 2014. Scikit-image: Image processing in Python. *PeerJ*, 2: e453.

Yang, X., Mühlhausen, M. P., Fröhlich, J. 2021a. Interpolation methods for two-way coupled Euler–Lagrange simulation of finite-size bubbles. *Chemical Engineering Science*, 238: 116566.

Yang, X., Mühlhausen, M. P., Fröhlich, J. 2021b. Efficient simulation of bubble dispersion and resulting interaction. *Experimental and Computational Multiphase Flow*, 3: 152–170.